

Computational screening of cathode materials for Zn-ion rechargeable batteries

Sriram Anand,^{†,‡} Caio Miranda Miliante,[†] Storm Gourley,[¶] Brian D. Adams,[§]
Drew Higgins,[¶] and Oleg Rubel^{*,†}

[†]*Department of Materials Science and Engineering, McMaster University, 1280 Main
Street West, Hamilton, Ontario L8S 4L8, Canada*

[‡]*Department of Metallurgical and Materials Engineering, National Institute of Technology
Tiruchirappalli, Tamil Nadu 620015, India*

[¶]*Department of Chemical Engineering, McMaster University, 1280 Main Street West,
Hamilton, Ontario L8S 4L8, Canada*

[§]*Salient Energy Inc., Dartmouth, Nova Scotia B3B 1C4, Canada*

E-mail: rubelo@mcmaster.ca

Abstract

We propose a comprehensive set of indicators (including methods to obtain and analyse them) for computational screening of candidate cathode materials for rechargeable Zn-ion aqueous batteries relying on Zn^{2+} intercalation processes. The indicators capture feasibility of Zn^{2+} intercalation and transport within the material, the thermodynamic stability of charged and discharged material structures, electrochemical stability of the cathode material and electrolyte, volume expansion, and energy storage capacity. The approach was applied to well-known cathode materials ($\alpha\text{-MnO}_2$ and $\alpha\text{-V}_2\text{O}_5$) as well as several potential alternatives (MoS_2 , ZrP_2O_7 , MoO_3 , and FeO_2) to demonstrate the screening workflow and the decision making process. We

show that selection of cathode materials for Zn-ion aqueous rechargeable batteries is a multifaceted problem, and first principle calculations can help to narrow down the search. Despite us being unable to identify a particularly successful cathode material, tools and techniques developed in this work can be applied more broadly to screen a wider array of potential material compositions and structures, with the goal of identifying next generation cathode materials for aqueous rechargeable batteries with the intercalation energy storage mechanism not limited to Zn^{2+} ions.

1 Introduction

Owing to their light-weight, high energy density and long-term cyclability, lithium ion (Li-ion) batteries have become front-runners for energy storage in handheld devices and electric vehicles. However, the scarcity of raw materials reduces their economic feasibility, and the flammability and toxicity of the electrolytes used adds further concerns of operational safety.^{1,2} Recently, the focus of battery research has broadened towards multivalent ion batteries, such as Zn^{2+} , Mg^{2+} and Al^{3+} .^{3,4}

Rechargeable aqueous zinc-ion batteries (RAZIBs) offer several benefits in terms of the balance of performance, cost, environmental impact and material abundance, and consequently stand apart from current battery technologies.⁵ Two major bottlenecks to the progress and commercial realization of RAZIBs are the electrochemical stability of the cathode during the intercalation-deintercalation cycles and risk of electrolyte oxidation (i.e., the oxygen evolution reaction).⁶

Oxides of manganese have been previously studied⁶⁻¹⁰ for application as RAZIB cathodes due to their abundance, ease of processing and eco-friendly nature. The main concern of RAZIBs is the electrochemical stability of the cathode material (dissolution of Mn^{2+} into the electrolyte and co-deposition of non-stoichiometric manganese oxides) that is responsible for capacity fade over time.^{2,6,8,11-13} Vanadium based cathodes gained recognition for their excellent capacity retention, especially the layered $\alpha\text{-V}_2\text{O}_5$ cathode, however, these mate-

rials are more expensive and as cathodes produce low discharge voltages relative to MnO_2 , making them less favourable in applications that require high voltages and energy density.² Prussian blue analogues are another prominent class of cathodes with tested discharge potentials of ca. 1.7 V. However, for the purpose of this study, they are not considered due to their low specific capacities.⁶ Discovery of cathode materials that mitigate such drawbacks is hence of great importance for large-scale realization of RAZIBs.

Previously, cathode materials for Li-ion batteries^{14,15} and multivalent ion batteries¹⁶ have been modeled to determine their discharge potentials by estimating the energy associated with the working ion insertion using the density functional theory (DFT).^{17,18} A Battery Explorer application in the Materials Project¹⁹ allows screening of cathode materials candidates using the charge potential and several complementary indicators, such as the theoretical specific capacity, the volume change as well as stability of charged and discharged materials relative to the energy convex hull. Feasibility of kinetic processes within the cathode material can be indirectly evaluated by determining the diffusion barrier for the charged ion migration also with DFT.²⁰ However, the electrochemical stability of cathode materials remains overlooked in existing screening protocols.

Exploration and screening of suitable RAZIB cathode materials can also be expedited by providing theoretical estimates of thermodynamic characteristics associated with Zn^{2+} intercalation. To date computational efforts in the field of RAZIB cathode materials are scarce. Le et al.²¹ reported calculations of the Zn^{2+} deintercalation potential in $\alpha\text{-MnO}_2$ showing that hydration along with the Hubbard U correction in DFT are important factors for reproducing the experimental intercalation potential. Our group showed that it is possible to reproduce the experimental deintercalation potential in electrolytic MnO_2 at the PBE+ U level of theory using the spinel ($\lambda\text{-Zn}_{0.1}\text{Mn}_2\text{O}_4$) structure as a model without hydration.¹³ (Here PBE stands for Perdew, Burke, and Ernzerhof²² exchange-correlation functional.) Luo et al.²³ recently reported high-throughput screening of spinel materials with a general formula $XY_2\text{O}_4$ (where X and Y are metals with one of them being either

Mn or Zn) as cathodes in RAZIB. Their screening parameters were the Zn^{2+} intercalation potential, the volume change upon charge/discharge, the Zn^{2+} diffusion coefficient, the thermodynamic stability of the XY_2O_4 structure,²³ and zero band gap as an indicator of good electrical conductivity. Shortcomings of Ref. 23 are the omission of the Hubbard U correction leading to a mismatch between calculated and measured charge potentials, unrealistic spinel-derived $\text{Zn}_x\text{XY}_2\text{O}_4$ structures, and omission of the electrochemical stability analysis. This leaves a room for development of a comprehensive procedure for screening of RAZIB cathode materials using thermodynamic parameters computed with DFT or extracted from literature, which can adequately determine their real-world applicability.

In this paper, we used Zn/MnO_2 and $\text{Zn}/\text{V}_2\text{O}_5$ as well-studied rechargeable zinc-ion battery materials to verify and benchmark the predictive power of first-principle calculations. We propose a screening protocol that includes analysis of the structural features to allow kinetic insertion and extraction of Zn^{2+} ions, Zn^{2+} deintercalation potential, thermodynamic stability of the cathode in charged and discharge states, feasibility of synthesis of the pristine cathode material, energy storage capacity, volume change due to Zn intercalation, and electrochemical stability. We demonstrated the approach by applying the protocol to several potential cathode materials for RAZIBs with different redox active metal centers: FeO_2 , MoS_2 , ZrP_2O_7 , and MoO_3 . With this procedure we aim to significantly diminish the time for evaluating the characteristics of a potential cathode material, as it takes not more than one week to analyze a relatively simple structure (up to 50 atoms), while the experimental route spans any time between a few weeks to a few months.

2 Computational details

DFT calculations were performed using the Vienna *ab initio* simulation package (VASP).²⁴⁻²⁶ The generalized gradient approximation (GGA) with the Perdew-Burke-Ernzerhof (PBE)²² parametrization was used for approximating the exchange-correlation energy along with the

DFT-D3 method with Becke-Johnson damping^{27,28} to capture van der Waals interactions. Projector augmented wave pseudopotentials²⁹ were employed in all calculations. The Brillouin zone was sampled using a Monkhorst-Pack grid of k points³⁰ generated automatically with a linear density of 20 divisions per 1 \AA^{-1} of the reciprocal space. The plane wave cut-off energy specified by the pseudopotentials was increased by 25% to achieve an accurate stress tensor. The energy convergence threshold was set at 10^{-5} eV. We performed full structure relaxations for all compounds. The relaxation threshold for forces acting on atoms was set at 0.05 eV \AA^{-1} and for the stresses at 1 kbar. The initial magnetic ordering was assumed ferromagnetic with the exception of Mn compounds, where we explored alternative antiferromagnetic spin configurations. The effect of magnetic ordering (ferromagnetic vs antiferromagnetic) has a minor effect on total energies. For instance, the DFT PBE+D3+ U total energy per formula unit (f.u.) of α -MnO₂ changes from -21.509 eV/f.u. (antiferromagnetic) to -21.510 eV/f.u. (ferromagnetic).

To account for correlations effects the PBE exchange-correlation was augmented with a Hubbard U correction (a simplified approach introduced by Dudarev et al.³¹). The performance of DFT+ U for modelling transition-metal oxides and electrochemical reactions has been shown to be the more accurate method owing to better representation of localised valence d and f electrons.³² Here we adopted U_{eff} values benchmarked in Ref. 33 for the transition metal (TM) elements listed in Table 1 throughout all compounds where they are present.

Table 1: Hubbard PBE+ U parameters for d electrons of TM species taken from Ref. 33. The single parameter $U_{\text{eff}} = U - J$ is used according to Dudarev et al.³¹ DFT+ U approach.

Element	U_{eff} (eV)
Mn	3.9
V	3.1
Fe	4.0
Mo	3.5

A nudged elastic band (NEB) method^{34,35} was used to calculate the Zn diffusion energy barrier between its favored intercalation position in a unit cell for the benchmark materials,

α -V₂O₅ and α -MnO₂. VASP’s implementation of the method^{34,35} was used with the spring constant set to -5 and 16 intermediate ‘images’ between the initial and final points. To improve convergence of the NEB path for α -V₂O₅, the search for a minimum energy paths was initially executed without the Hubbard U correction. Then, the calculated images were used as a starting point for the final calculation with the Hubbard U correction.

The central thermodynamic quantity for analysis of stability of materials is the formation energy. It is calculated (in eV per f.u.) using the expression

$$\Delta H_f = H(\text{compound}) - \sum_i^{\text{elements}} N_i H(i, \text{bulk}), \quad (1)$$

where the summation index i runs over all constituting elements of the compound, H stands for DFT total energies (per f.u. for the compound or per atom for individual elements), and N is the number of atoms i in the compound (per f.u.). The elemental solids (or molecules) are considered in their most stable form. The pressure times volume (PV) enthalpy term is ignored. It only reaches a sizable magnitude for O₂ gas still contributing only 0.023 eV per molecule, which is an order of magnitude smaller than the chemical accuracy of PBE (see Table 2).

Table 2: Formation energies (eV/f.u.) of cathode materials computed using Eq. (1) compared with experimental enthalpies and other calculations reported in literature.

Material	PBE+D3	PBE+D3+ U	Experimental	Calculated (literature)
β -MnO ₂	-5.07	-4.66	-5.39 ³⁶	-4.78 (PBE) ³⁷ -5.07 (PBE) ³⁸ -4.63 (PBE+ U = 3 eV) ³⁷
α -MnO ₂	-5.02	-4.69	—	-5.42 (ID: mp-19395) ¹⁹
λ -MnO ₂	-4.85	-4.56	—	-4.91 ³⁸
α -V ₂ O ₅	-15.62	-15.73	-16.07 ³⁹	-16.11 (PBE) ⁴⁰ -16.03 (PBE+D3+ U = 3.5 eV) ⁴⁰
α -FeO ₂	—	-3.85	—	-3.73 (ID: mp-796324) ¹⁹
λ -FeO ₂	—	-3.37	—	-3.31 (ID: mp-540003) ¹⁹
MoO ₃	—	-7.95	-7.72 ³⁹	-7.54 (ID: mp-20589) ¹⁹
MoS ₂	—	-2.52	-2.86 ³⁹	-3.61 (ID: mp-2815) ¹⁹
ZrP ₂ O ₇	-27.0	—	-27.4 ⁴¹	-31.07 (ID: mp-5024) ¹⁹

The insertion of Zn should be energetically favorable for a cathode material to be a viable candidate. We assess this by calculating the corresponding energy (in eV per Zn atom)

$$\Delta H_{\text{Zn}} = \frac{H(\text{Zn}_x\text{M}_y\text{O}_z) - H(\text{M}_y\text{O}_z) - xH(\text{Zn})}{x} \quad (2)$$

based on PBE+D3+*U* total energies H . Negative value of ΔH_{Zn} indicates favorable Zn insertion.

The Zn^{2+} deintercalation potential of a $\text{Zn}_x\text{M}_y\text{O}_z$ compound is obtained from the Nernst equation

$$E \approx -\frac{\Delta H_{\text{Zn}}}{n_e e}, \quad (3)$$

where n_e is the number of electrons transferred per ion (2 for Zn^{2+}) and e is the elementary charge. This expression is equivalent to that originally proposed by Aydinol et al.¹⁵. Here we neglect finite temperature effects assuming that they largely cancel out thus the approximate sign in Eq. (3).

The theoretical specific capacities of a cathode material $\text{Zn}_{0\dots x}\text{M}_y\text{O}_z$ was computed using the relation⁴²

$$C = \frac{x n_e F}{3.6 M_w}, \quad (4)$$

where F is the Faraday constant and M_w is the molar mass of the host compound M_yO_z . The factor 3.6 accounts for units conversion to yield mA h g^{-1} .

3 Results and Discussion

3.1 Validation of methods using Zn/ V_2O_5 and Zn/ MnO_2

Zn/ MnO_2 and Zn/ V_2O_5 systems are taken as benchmarks for the purpose of this study owing to prior experimental works on their use as RAZIB cathodes.^{43–47} Crystal structures corresponding to a discharged state (with intercalated Zn) are presented in Fig. 1. In addi-

tion to the standard spinel ZnMn_2O_4 phase, the structure of hollandite-like ZnMn_2O_4 was derived from $\alpha\text{-MnO}_2$ by placing Zn inside tunnels. Multiple alternative Zn arrangements were tested in attempt to achieve an optimal coordination of Zn atoms. The lowest energy structure is presented in Fig. 1(b), which is similar to the one suggested computationally in Ref. 21. It should be noted, however, that there is no experimentally resolved hollandite-like ZnMn_2O_4 structure reported in the literature. Similarly, there is no native ZnV_2O_5 structure. The derived structure of ZnV_2O_5 (Fig. 1c) was inspired by the experimental atomic-resolution studies of Zn insertion in $\alpha\text{-V}_2\text{O}_5$.⁴⁸

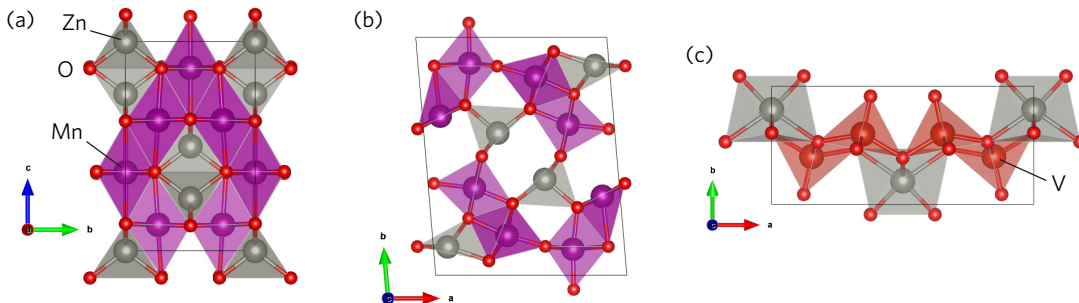


Figure 1: Benchmark structures with intercalated Zn: (a) spinel ZnMn_2O_4 , (b) hollandite-like ZnMn_2O_4 , and (c) layered ZnV_2O_5 .

Calculated structures of materials used in the benchmark study ($\alpha, \lambda\text{-MnO}_2$, spinel ZnMn_2O_4 , and $\alpha\text{-V}_2\text{O}_5$) are compared to experiment in Table 3. Structures computed using PBE+D3 exchange-correlation functional have an average error of 0.2% in lattice parameters (1.2% maximum absolute error), while PBE+D3+ U achieves a greater average error of 0.8% in lattice parameters (2.2% maximum absolute error). This level of accuracy is within limits expected for DFT with semilocal exchange-correlation functionals.⁴⁹

Chemical accuracy of DFT calculations was tested by computing the formation energies ΔH_f of benchmarked compounds and comparing them with experiments as well as calculated values reported in literature (Table 2). Both choices for the exchange-correlation functional (PBE+D3 and PBE+D3+ U) systematically underestimate ΔH_f for oxides which is consistent with numerous prior studies.^{33,37,38} Even though the addition of a Hubbard correction

Table 3: Calculated lattice parameters of materials compared with experimental data from a Springer Materials database⁵⁰ (a unique database identifier is given in brackets).

Material	Space group	Method	Lattice parameters (Å)
α -MnO ₂	I4/m (87)	PBE+D3	$a = 9.75, c = 2.86$
		PBE+D3+ U	$a = 9.82, c = 2.91$
		Exp. (sd_0542154)	$a = 9.815, c = 2.847$
λ -MnO ₂	Fd $\bar{3}$ m (227)	PBE+D3	$a = 8.09$
		PBE+D3+ U	$a = 8.18$
		Exp. (sd_1142474)	$a = 8.060$
ZnMn ₂ O ₄	I4 ₁ /amd (141)	PBE+D3	$a = 5.73, c = 9.29$
		PBE+D3+ U	$a = 5.78, c = 9.34$
		Exp. (sd_0377570)	$a = 5.772, c = 9.236$
α -V ₂ O ₅	Pmmn (59)	PBE+D3	$a = 11.65, b = 3.57, c = 4.37$
		PBE+D3+ U	$a = 11.73, b = 3.62, c = 4.28$
		Exp. (sd_0313359)	$a = 11.510, b = 3.563, c = 4.369$
MoO ₃	Pnma (62)	PBE+D3+ U	$a = 14.71, b = 3.72, c = 3.88$
		Exp. (sd_0530932)	$a = 14.02, b = 3.703, c = 3.966$
MoS ₂	P6 ₃ /mmc (194)	PBE+D3+ U	$a = 3.17, c = 12.24$
		Exp. (sd_0309036)	$a = 3.16, c = 12.29$
ZrP ₂ O ₇	Pa $\bar{3}$ (205)	PBE+D3+ U	$a = 8.50$
		Exp. (sd_1222320)	$a = 8.272$

U does not lead to improving ΔH_f , however, it does improve the description of correlation effects in localized orbitals of TM oxides and allows to get oxidation energies (and, therefore, redox energies) correctly⁵¹ which becomes important later when calculating a Zn²⁺ deintercalation potential and charge voltage.

With formation energies at hand, we can verify stability of intercalated structures. However, it is not sufficient to claim stability based on the negative formation energy alone. It is important to perform a energy convex hull analysis and verify that the material in question ($\text{Zn}_x\text{M}_y\text{O}_z$) is *on* the convex hull. For this purpose, we plot a section of the ternary convex hull Zn– $M_y\text{O}_z$. Assuming that $M_y\text{O}_z$ is stable, we can define a relative stability parameter δH (in eV per atom)

$$\begin{aligned}
 \delta H &= \frac{H(\text{Zn}_x\text{M}_y\text{O}_z) - H(\text{M}_y\text{O}_z) - xH(\text{Zn})}{x + y + z} \\
 &= \frac{\Delta H_f(\text{Zn}_x\text{M}_y\text{O}_z) - \Delta H_f(\text{M}_y\text{O}_z)}{x + y + z}.
 \end{aligned} \tag{5}$$

Here we replaced the total energies H with formation energies ΔH since such values are also available experimentally. Negative values of δH suggest that Zn insertion is favorable. The $\text{Zn}_x\text{M}_y\text{O}_z$ compound is considered stable if it has the lowest δH among other polymorphs of the same compound or combination of other compounds with equivalent composition, which makes this analysis analogous of the energy convex hull.

The relative stability parameter δH is presented in Fig. 2. The spinel ZnMn_2O_4 is the most stable structure being on the convex hull, while hollandite-like ZnMn_2O_4 and ZnV_2O_5 are metastable since they are above the convex hull with yet negative δH . Results with and without the Hubbard U correction are qualitatively the same. Quantitatively, PBE+D3+ U results in a more discern convex hull and significantly more negative δH making Zn intercalation even more favorable.

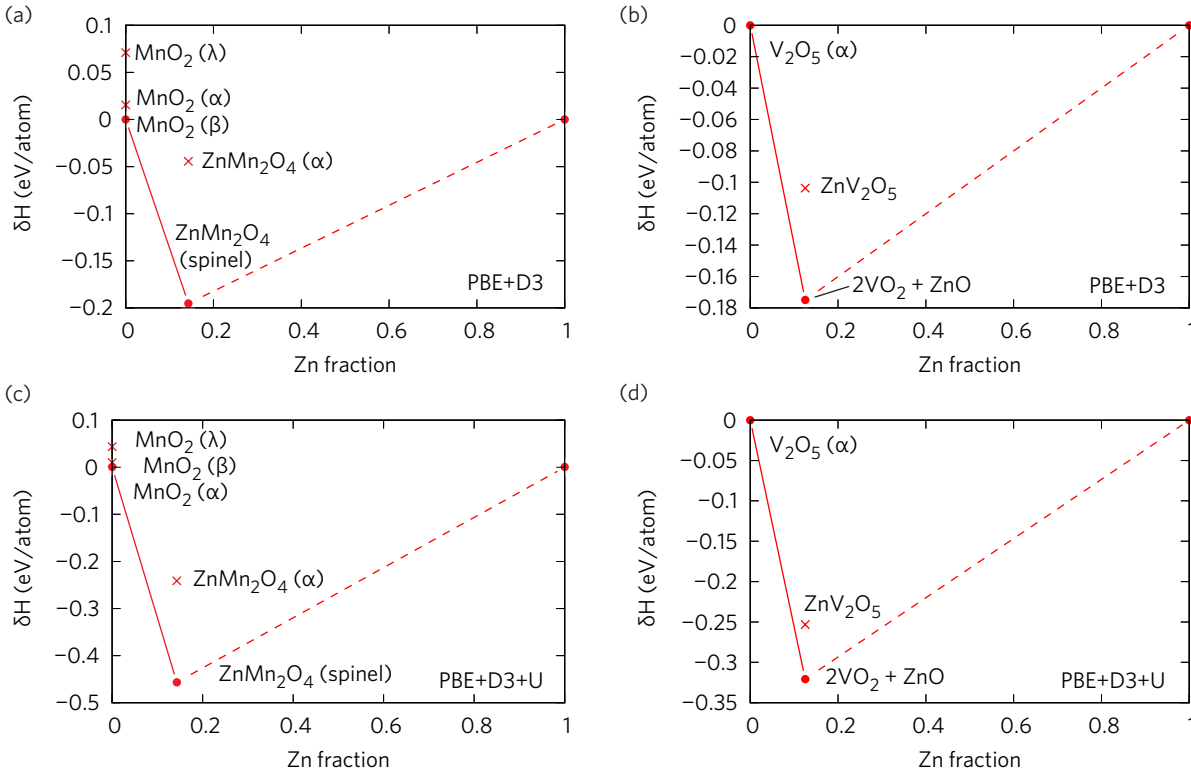


Figure 2: MnO_2 -Zn and V_2O_5 -Zn energy convex hull diagrams: (a,b) computed at the PBE+D3 level of theory, (c,d) computed at the PBE+D3+ U level of theory.

The Zn^{2+} deintercalation potential vs $\text{Zn}^0/\text{Zn}^{2+}$ calculated according Eq. (3) for the benchmark structures in Fig. 1 are listed in Table 4. Calculations without the Hubbard

U correction systematically underestimate the Zn^{2+} deintercalation potential. Inclusion of the Hubbard U correction is essential to reproduce experimental deintercalation potentials as also evident from prior studies of cathode materials for Li-ion batteries^{14,52} since PBE exchange-correlation functional systematically underestimates the intercalation and redox potentials.^{14,33} The correction compensates inaccuracy of the semi-local PBE exchange-correlation potential and lowers energy of d states at the TM ion. As a result, calculations reproduce more accurately an energy gained by the transfer of electrons from Zn to the TM ion. For this reason PBE+D3+ U will be used to evaluate alternative cathode materials for the remainder of this paper.

Table 4: Zn^{2+} deintercalation potentials (V) vs $\text{Zn}^0/\text{Zn}^{2+}$ for benchmark structures in Fig. 1 computed with and without the Hubbard correction U . The average experimental Zn extraction and insertion potential are listed for comparison.

Cathode	TM redox couple	PBE+D3	PBE+D3+ U	Experimental
$\lambda\text{-MnO}_2$	$\text{Mn}^{4+/3+}$	0.9	1.7	1.5 ± 0.5 ^{53,54}
$\alpha\text{-MnO}_2$	$\text{Mn}^{4+/3+}$	0.3	1.1	1.5 ^{43,55,56}
$\alpha\text{-V}_2\text{O}_5$	$\text{V}^{5+/4+}$	0.4	1.0	$0.8,$ ^{45,57} 1.0 ⁵⁸

Despite applying the U correction, we are unable to fully recover the experimental potential for $\alpha\text{-MnO}_2$ (Table 4). We attempted to include hydration of Zn ions to achieve their proper coordination within the $\alpha\text{-MnO}_2$ structural voids, but it did not improve the agreement with experiment (see Sec. 3.2). Other mechanisms contributing to the energy storage (MnO_2 dissolution or H^+ intercalation) can mask Zn^{2+} intercalation as they occur within the same potential window.^{11,13,59-61} Thus, the spinel phase gives a better representation of ZnMn_2O_4 thermodynamics at DFT level than its hollandite-like counterpart. There is other evidence suggesting structural instabilities of highly loaded $\alpha\text{-MnO}_2$: Large distortions of α -like K_xMnO_2 ($x > 0.25$) was reported by Jiao et al.⁶² who attributed it to a transformation from a tunnel to a layered structure (we can see that in Fig. 1(b) as well). Le et al.²¹ in DFT studies observed structural transformation and transition from α to a layered δ structure starting at $\text{Zn}_{0.375}\text{MnO}_2$.

In order to investigate how facile Zn^{2+} transport can be expected during intercalation into the cathode material, its diffusion energy barrier in $\alpha\text{-V}_2\text{O}_5$ and $\alpha\text{-MnO}_2$ was calculated. The converged path for Zn^{2+} diffusion and its associated energy profile can be seen on Fig. 3 for both materials. For these simulations supercells with only one Zn atom were constructed, which resulted in $\text{ZnV}_4\text{O}_{10}$ and $\text{ZnMn}_8\text{O}_{16}$ stoichiometries. A full structure relaxation was performed for these compounds previous to the NEB calculation, so as to correctly capture its favourable intercalation ordering. The calculated energy barriers for Zn^{2+} diffusion in $\alpha\text{-V}_2\text{O}_5$ and $\alpha\text{-MnO}_2$ were of 1.0 and 0.1 eV, respectively. The large barrier height disparity can be linked to structural differences between the materials. $\alpha\text{-V}_2\text{O}_5$ is a layered system in which Zn strongly interacts with both layers on its minimal energy path (Fig. 3c). In contrast, the characteristic 2×2 tunnels of $\alpha\text{-MnO}_2$ have more space, and Zn atoms are partly bonded to one side of the tunnel (Fig. 3a).

A comparison can be made with other reported energy barriers for Zn^{2+} diffusion within the systems analysed here. Prior first-principle studies reported much lower values of the barrier 0.305 eV⁶³ and 0.584 eV⁶⁴ for $\alpha\text{-V}_2\text{O}_5$ based on DFT-PBE calculations. The discrepancy for $\alpha\text{-V}_2\text{O}_5$ can be partially explained by omission of the Hubbard U correction in Refs. 63,64. We observed a decrease of the energy barrier by ca. 25% when the U correction is not applied. Another aspect is related to structural distortions of the host $\alpha\text{-V}_2\text{O}_5$ lattice in response to Zn insertion. As can be seen on Fig. 1(c) for ZnV_2O_5 and Fig. 3(c) for $\text{ZnV}_4\text{O}_{10}$, the $[\text{VO}_5]$ pyramids get tilted upon Zn insertion in attempt to establish Zn–O bonds. This phenomenon is well documented for intercalation of other ionic species (e.g., Li^+ and Mg^{2+} ^{65,66}) in $\alpha\text{-V}_2\text{O}_5$. These structural distortions impede a direct linear diffusion path between the layers, thus resulting in a curved S -shaped path with a larger barrier. Graphical images presented in Refs. 63,64 suggest that such structural distortions due to Zn presence could have been omitted in prior works, while the lack of calculated structures therein precludes us from reproducing data (see Sec. “Supporting Information Available” for data availability pertaining to this work). In the case of $\alpha\text{-MnO}_2$, Putro et al.⁶⁷ reported

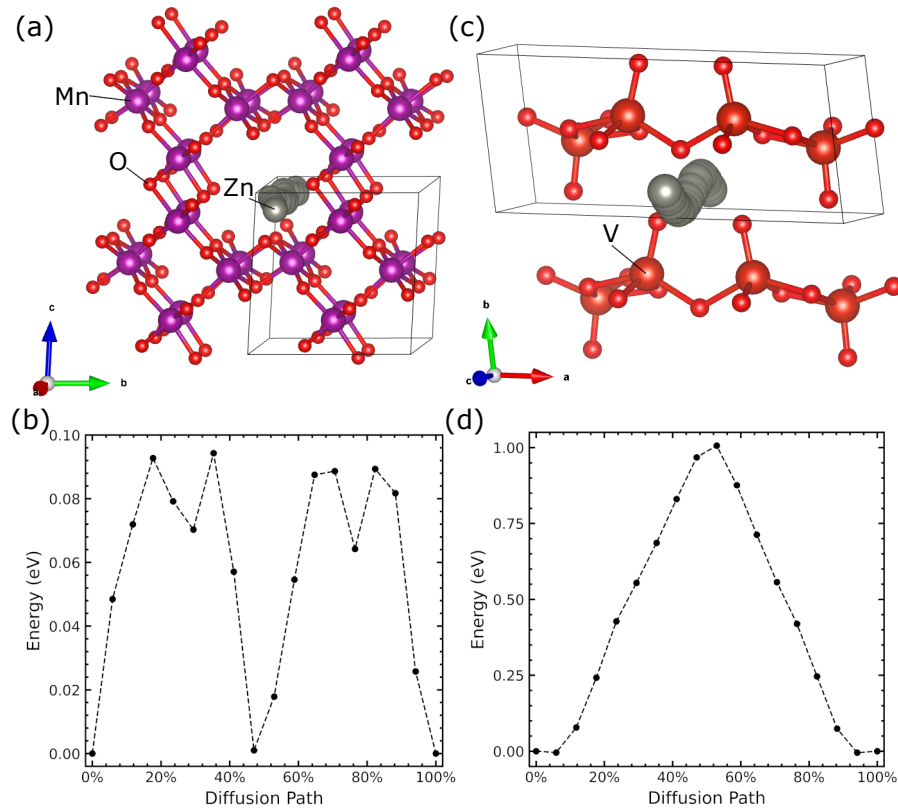


Figure 3: NEB lowest energy path for Zn^{2+} diffusion in α - MnO_2 (a, b) and α - V_2O_5 (c, d). The relative PBE+D3+ U total energy change along the path allows to evaluate the diffusion energy barrier.

the barrier of 0.34 eV for Zn migration evaluated on a path that follows through the centre of the characteristic 2×2 void rather than selecting energetically more preferable coordination of the add-atom.

Rong et al.⁶⁸ arrived to 0.525 eV as a reference maximum value for an intercalated ion energy barrier by analyzing different aspects pertaining to Li-ion batteries, for example its (dis)charge rate and active material size, when considering the ion diffusion as a random walk. From this we would expect efficient Zn intercalation in $\alpha\text{-MnO}_2$ only. As the energy barrier for $\alpha\text{-V}_2\text{O}_5$ is an order of magnitude higher, we can anticipate the Zn^{2+} diffusion in $\alpha\text{-V}_2\text{O}_5$ to be drastically different (10^{15} fold slower at the room temperature). However, numerous experiments^{2,6,9,69} evidence that both materials demonstrate similar performance as cathodes for RAZIB. The discordance between the barrier height and performance of $\alpha\text{-MnO}_2$ and $\alpha\text{-V}_2\text{O}_5$ cathode materials calls for dissolution and subsequent re-deposition of the cathode material in the aqueous electrolyte as possible alternative energy storage mechanism (following Refs. 2,6) that is not sensitive to Zn diffusion. Eventually, we are unable to conclude on the barrier height as a useful design metric for RAZIB cathode materials.

3.2 Role of hydration in incorporation of Zn

Here we explore the role of hydration in incorporation of Zn^{2+} ions in $\alpha\text{-MnO}_2$ with the hope to improve the agreement with experiment (Table 4). Calculations of Zn^{2+} deintercalation potential were performed for structures shown in Fig. 4. Those structures represent stoichiometry of a fully charged (Fig. 4a), a half discharged hydrated (Fig. 4b) and anhydrous (Fig. 4c) states. The partly discharged state was used as it was not possible to accommodate more Zn ions and water molecules at the same time.

By comparing the total energies of $\alpha\text{-Mn}_4\text{O}_8 \cdot \text{H}_2\text{O}$ with the anhydrous $\alpha\text{-MnO}_2$ and solid water, we conclude that the hydration enthalpy is ca. 0.4 eV per H_2O molecule. The positive enthalpy suggests that incorporation of water is energetically unfavourable. Similar comparison of total energies for structures with zinc $\text{ZnMn}_4\text{O}_8 \cdot \text{H}_2\text{O}$ vs ZnMn_4O_8 and solid

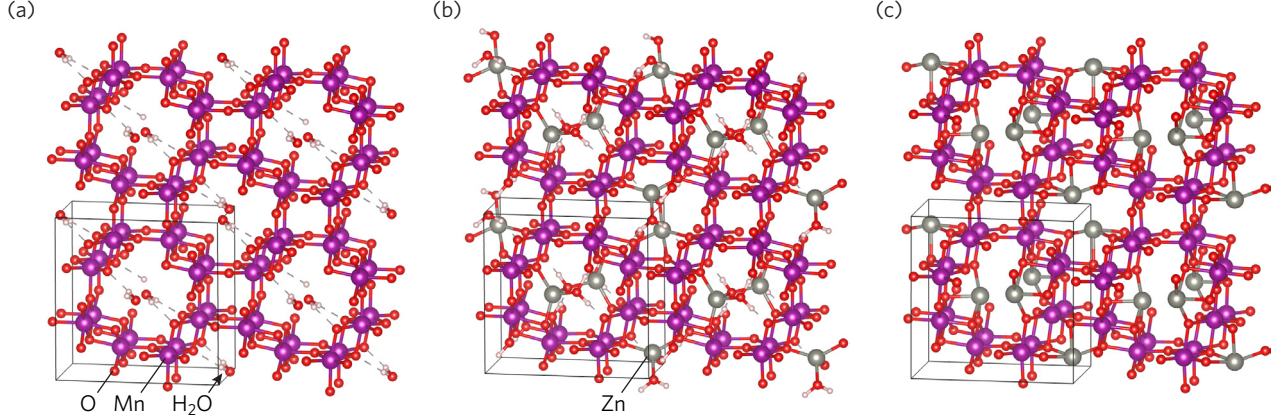


Figure 4: Structures of (a) $\alpha\text{-Mn}_4\text{O}_8 \cdot \text{H}_2\text{O}$, (b) $\text{ZnMn}_4\text{O}_8 \cdot \text{H}_2\text{O}$, and (c) ZnMn_4O_8 .

water yields the hydration enthalpy of 0.13 eV per H_2O molecule. This trend indicates that the hydration becomes more favourable when accompanied by intercalation of Zn.

Using total energies of the structures in Fig. 4a,b for the charged and discharged phases, respectively, we obtained the Zn^{2+} deintercalation potential of 1.0 V vs $\text{Zn}^0/\text{Zn}^{2+}$ at the PBE+D3+ U level of theory. As a reference, we also evaluated the Zn^{2+} deintercalation potential for the very similar anhydrous structure (Fig. 4c) as 0.9 V vs $\text{Zn}^0/\text{Zn}^{2+}$. Even though the coordination of Zn ions is improved in the hydrated structure, the hydration does not improve the agreement with experiment for the Zn^{2+} deintercalation potential (Table 4), contrary to calculations carried out by Le et al.²¹. It should be noted that Ref. 21 considered a higher number of incorporated water molecules, which resulted in breaking the characteristic $\alpha\text{-MnO}_2$ 2×2 tunnels. This could explain their ability to achieve a greater Zn^{2+} deintercalation potential. However, to the best of our knowledge, the literature lacks reports supporting either of those α -like $\text{Zn}_x\text{MnO}_2 \cdot y\text{H}_2\text{O}$ structures derived directly from experimental crystallographic techniques. Hence, our analysis of hydrated structures was limited to those where the structural features of $\alpha\text{-MnO}_2$ were preserved.

3.3 Selection of alternative cathode materials

We selected two layered materials (MoS_2 and MoO_3) and two materials with tunnels or voids (ZrP_2O_7 and $\alpha\text{-FeO}_2$) as shown in Fig. 5. This selection represents TM oxides and sulfides with a crystal structures suitable to host Zn (the atomic diameter of Zn is 2.7 \AA ⁷⁰). The initial crystal structures were obtained from Springer Materials⁵⁰ or the crystallography open database.^{71–73} ZrP_2O_7 (Fig. 5b) and $\alpha\text{-FeO}_2$ (Fig. 5d) have voids of the size 3.1 and 4.1 \AA , respectively. For comparison, $\alpha\text{-MnO}_2$ has the tunnel size of 3.9 \AA based on Slater⁷⁰ atomic radii.

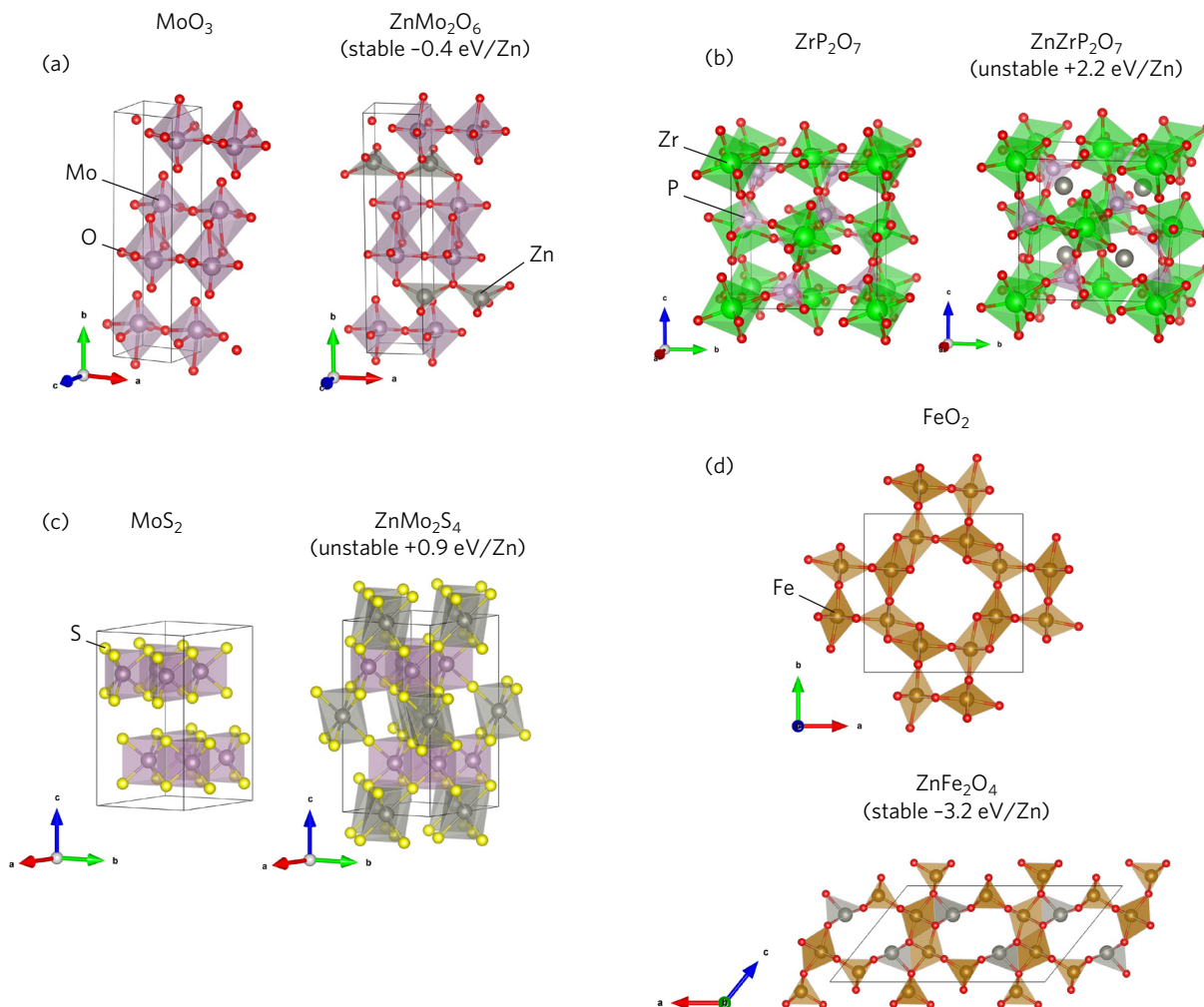


Figure 5: Structures of alternative cathode materials without and with intercalated Zn: (a) MoO_3 and ZnMo_2O_6 , (b) ZrP_2O_7 and ZnZrP_2O_7 , (c) MoS_2 and ZnMo_2S_4 , (d) $\alpha\text{-FeO}_2$ and α -like ZnFe_2O_4 . Feasibility of Zn intercalation is expressed as energy per Zn atom calculated using Eq. (2) at PBE+D3+ U level.

Alternatively, the intercalation of Zn^{2+} can take place via intercalation of the hydrated ion.^{45,56,74-76} Cauët et al.⁷⁷ concluded that the first hydration shell involves six water molecules arranged in an octahedral geometry $\text{Zn}^{2+} + 6 \text{H}_2\text{O}$ (see Fig. 7 therein). Therefore, we can estimate diameter of the first hydration shell as 6.7 Å based on the $\text{Zn}^{2+} - \text{O}_1$ distance of 2.1 Å,⁷⁷ the $\text{O}_1 - \text{H}$ distance of 1 Å, and the hydrogen radius of 0.25 Å.⁷⁰ Given the size of the hydration shell, only layered structures have enough spacing to accommodate fully hydrated Zn^{2+} ions.

The choice of $\alpha\text{-FeO}_2$ was inspired by Brady et al.⁷⁸ who explored possibilities of TM substitutions in $\alpha\text{-MnO}_2$. There are two minerals Akaganeite and Schwertmannite with the $\alpha\text{-FeO}_2$ tunnel structure,^{79,80} however both are minerals of Fe(III); Fe(IV)-oxides do not occur in nature. The spinel phase of ZnFe_2O_4 exists and showed some performance in Li-ion batteries.⁸¹ However, its narrow tunnels (2.1 Å) are not ideal for reversible transport of Zn^{2+} ions.

3.4 Zn intercalation affinity

There are no experimental structures of MoS_2 , MoO_3 , ZrP_2O_7 , and FeO_2 with Zn that would closely resemble the pristine structure. Zn intercalation sites were chosen after inspecting voids in the host structures. When placing Zn into the structure we tried to match its natural coordination (four-, five-, and six-fold) when possible. Subsequently, all structures were fully relaxed to minimize forces and stresses.

Structures of cathode materials with and without Zn are shown in Fig. 5. Upon Zn insertion all structures retained their similarity to the host material with the exception of $\alpha\text{-ZnFe}_2\text{O}_4$ (Fig. 5d). We observed this behaviour also in $\alpha\text{-ZnMn}_2\text{O}_4$ (Fig. 1b) and attributed it to a transformation from the structure with tunnels to a layered structure similar to $\alpha\text{-K}_x\text{MnO}_2$ structures.⁶²

The Zn intercalation energy (ΔH_{Zn}) calculated according to Eq. (2) is given alongside of each structure in Fig. 5. After evaluating the Zn intercalation energy, we conclude that

MoS₂/ZnMo₂S₄ and ZrP₂O₇/ZnZrP₂O₇ are not suitable for hosting Zn. This result corroborates failed experimental attempts to observe Zn intercalation and energy storage in unmodified MoS₂.⁸² However, there are other reports of successful Zn intercalation in a modified MoS₂ with defects (transition-metal vacancies)^{83,84} or a metastable (metallic) phase 1T'.⁸⁵ In the case of defects Zn passivates them. For example, two Zn²⁺ ions absorbed per one Mo⁴⁺ vacancy, which is possible in layered structures. However, the defect concentration should be very high to reach a significant capacity, which raises concerns about the structural integrity of the crystal. We continue with FeO₂/ZnFe₂O₄ and MoO₃/ZnMo₂O₆ as potential candidates.

3.5 Volume change upon Zn intercalation

Any volumetric changes within the cathode material provide insight into the cyclic stability and longevity of the battery. Large distortions and volume changes during charge or discharge can lead to uneven strain within the cathode material causing poor mechanical stability, cracking and capacity fading.⁸⁶ In Li-ion commercial batteries the volume change of the cathode material does not exceed 8% upon lithiation.⁸⁷ We will take this value as a guideline in our study, however we treat deviations as a warning rather than a requirement for materials selection.

The unit cell of α -MnO₂ and FeO₂ undergoes drastic changes upon Zn intercalation (Figs. 1b and 5d), even though the overall volume change is only 9% (Table 5). This renders both materials as prone to mechanical instabilities along with α -V₂O₅ which has a large volume change. Among all cathode materials in this study only MoO₃ falls within the acceptable volume change (under 8%) during Zn intercalation-deintercalation.

3.6 Zn²⁺ deintercalation potentials

We computed the average charge (or deintercalation) potential according to Eq. (3) for cathode materials that showed a favorable Zn intercalation. The deintercalation potential

Table 5: Summary of characteristics for cathode materials. All computational values correspond to PBE+D3+ U level of theory. Problematic entries are highlighted in bold.

Characteristic	α -MnO ₂	α -V ₂ O ₅	MoS ₂	ZrP ₂ O ₇	MoO ₃	FeO ₂
Structural feature	tunnels 2×2	layered	layered	cavity	layered	tunnels 2×2
Thermodynamic stability without Zn (eV/atom above hull)	0	0	0	0	0	0.25
Feasible to synthesise without Zn	yes	yes	yes	yes	yes	no
Zn insertion per formula unit (atom)	0.5	1	0.5	1	0.5	0.5
Energy storage capacity (mA h g ⁻¹)	310	300	170	200	190	310
Redox couple	Mn ^{4+/3+}	V ^{5+/4+}	Mo ^{4+/3+}	Zr ^{4+/2+}	Mo ^{6+/5+}	Fe ^{4+/3+}
Zn intercalation energy (eV/Zn)	-2.2	-2.0	+0.9	+2.2	-1.4	-3.2
Thermodynamic stability with Zn (eV/atom above hull)	0.21	0.07	—	—	0.14	0.18
Calculated charge potential (V vs Zn ⁰ /Zn ²⁺)	1.1 ^{+0.41}	1.0	—	—	0.7	1.6^{+0.4a}
Volume change upon Zn insertion (ln %)	9	15	—	—	4	9
Electrochemical stability: corrosion/dominance of another solid phase (% of area in Pourbaix diagram)	60/0	10/85	—	—	80/0	0/100
Charge potential is within the cathode electrochemical stability region	yes	no	—	—	no	no
Diffusion barrier (eV)	0.1	1.3	—	—	—	—

translates into the open circuit voltage measured against the zinc-metal anode ($\text{Zn}^0/\text{Zn}^{2+}$).

According to Eq. (3) the potential is 1.6 and 0.7 V vs $\text{Zn}^0/\text{Zn}^{2+}$ for $\alpha\text{-FeO}_2/\text{ZnFe}_2\text{O}_4$ and $\text{MoO}_3/\text{ZnMo}_2\text{O}_6$, respectively, at the PBE+D3+ U level of theory. Cyclic voltammetry of MoO_3 in a ZnSO_4 aqueous electrolyte shows oxidation and reduction peaks between 0.5 and 0.9 V vs $\text{Zn}^0/\text{Zn}^{2+}$.⁸²

We note increase in the theoretical charge potential from 1.1 (see Table 5) to 1.6 V vs $\text{Zn}^0/\text{Zn}^{2+}$ when substituting $\text{Mn}^{4+/3+}$ with $\text{Fe}^{4+/3+}$ in the hollandite-like structure. This trend is consistent with ordering of redox energies of 3d TM ion couples (see Fig. 1 in Ref. 88). Since PBE+D3+ U underestimated the experimental charge potential in $\alpha\text{-MnO}_2/\text{ZnMn}_2\text{O}_4$ by 0.4 V (see Table 4), we can expect a higher experimental charge potential (ca. 2 V vs $\text{Zn}^0/\text{Zn}^{2+}$) for the $\alpha\text{-FeO}_2/\text{ZnFe}_2\text{O}_4$ cathode material.

Considering the use of a mildly acidic aqueous electrolyte, the desired voltage range is from 1 to 1.8 V vs $\text{Zn}^0/\text{Zn}^{2+}$. The upper bound is governed by the oxygen evolution potential. Thus, oxides with the $\text{Fe}^{4+/3+}$ redox couple, in general, may not be suitable for Zn-ion rechargeable batteries with the aqueous electrolyte.

Calculations reported in this paper are performed without taking the aqueous medium into account explicitly. Shin et al.⁷⁴ reported that the computed voltages were higher in anhydrous V_6O_{13} and the voltages of hydrated structure overlapped with experimental results, while the voltages computed by Wu et al.⁸⁹ show the opposite trend of $\alpha\text{-V}_2\text{O}_5$ resulting in overestimation of the voltages in hydrated structures. However, intercalation cathodes have been modelled accurately without including the solvation sphere around the cation.⁶² Our own attempts reported in Sec. 3.2 did not improve calculations of the charge potential. Hence, the solvation sphere is not included in the computations.

We can conclude that MnO_2 , $\alpha\text{-V}_2\text{O}_5$, and MoO_3 have favourable charge potentials (Table 5).

3.7 Thermodynamic stability of structures before and after intercalation

Ideally, both the pristine cathode material and its Zn intercalated counterpart should show thermodynamic stability. So far, we used Eq. (2) to assess the Zn affinity. The negative value of the intercalation energy ΔH_{Zn} is a necessary condition for thermodynamic stability of the intercalated compound, but it is not a sufficient condition. To prove the thermodynamic stability we need to show that the intercalated compound is located on the energy convex hull. As of now, even previously successful cathode materials ($\alpha\text{-MnO}_2$ and $\alpha\text{-V}_2\text{O}_5$) were unable to meet this requirement for their Zn intercalated derivatives being 0.05–0.2 eV/atom above the hull (Fig. 2c,d) in DFT calculations at the PBE+D3+ U level of theory.

Figure 6a shows a ternary Zn–Mo–O phase diagram from the Materials Project^{33,90} obtained by a mixed PBE/PBE+ U scheme (including empirical corrections). The diagram correctly predicts major phases, such as MoO_2 , Mo_8O_{23} , MoO_3 , and ZnMoO_4 known experimentally,^{91–93} while failed to capture Mo_9O_{24} , Mo_4O_{11} , $\text{Zn}_2\text{Mo}_3\text{O}_8$, $\text{Zn}_3\text{Mo}_2\text{O}_9$. There is no stable phase with ZnMo_2O_6 stoichiometry which would represent the discharged state of the cathode material. According to the phase diagram (Fig. 6b) it would decompose into $\text{MoO}_2 + \text{ZnMoO}_4$ which places ZnMo_2O_6 into unstable position ca. 0.14 eV/atom above the convex hull (Fig. 6b).

Figure 7a shows a ternary Zn–Fe–O phase diagram from the Materials Project.^{33,90} The diagram correctly predicts phase Fe_3O_4 and Fe_2O_3 stable at ambient conditions, but also shows a high-temperature phase FeO .⁹⁴ The Materials Project data and also our own calculations in Fig. 7b preclude existence of the FeO_2 phase at ambient conditions (0.25 eV/atom above the hull), which correlates with experimental results.⁹⁵ The intercalated α -like ZnFe_2O_4 structure is also above the hull by 0.18 eV/atom, which applies to structures with an intermediate Zn content too. Thus, the Zn/ FeO_2 is the only couple where both intercalated and deintercalated structures are unstable.

It is instructive to put calculated energies relative to the convex hull in the context of

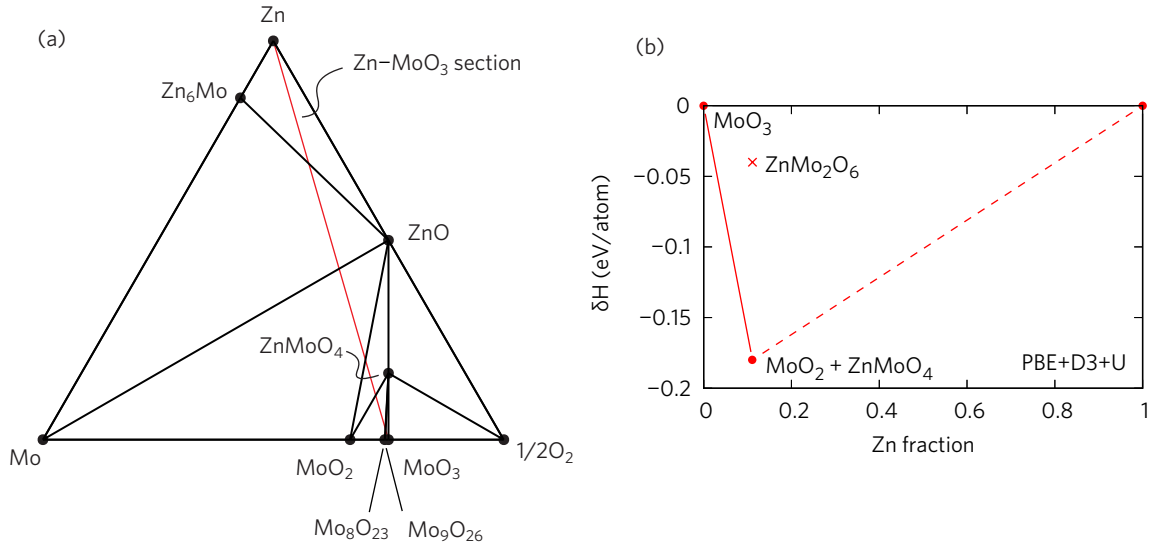


Figure 6: Phase diagrams: (a) Ternary Zn–Mo–O phase diagram reproduced from Materials project.^{33,90} (b) Zn–MoO₃ section of the phase diagram calculated in this work at the PBE+D3+*U* level.

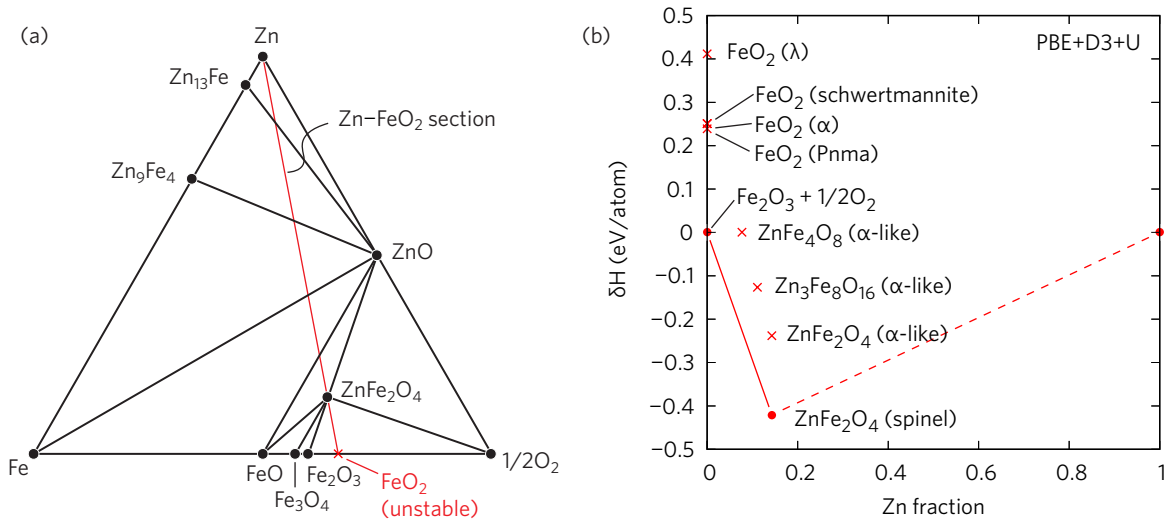


Figure 7: Phase diagrams: (a) Ternary Zn–Fe–O phase diagram reproduced from Materials project.^{33,90} (b) Zn–FeO₂ section of the phase diagram with Zn_{*x*}FeO₂ phases calculated in this work at the PBE+D3+*U* level.

existing battery materials. In the case of Li–Co–O ternary system, the layered LiCoO₂ phase is thermodynamically stable,⁹⁶ while the deintercalated CoO₂ structure is not. The CoO₂ solid is 0.16 eV/atom above the energy convex hull based on assessment of CALPHAD enthalpies presented in Table 3.2 of Ref. 97. Thus we can use this value as a threshold when the thermodynamic stability should raise a concern (bold values in Table 5). We can conclude that only α -V₂O₅ and MoO₃ meet expectations on their thermodynamic stability in charged and discharged states (Table 5).

3.8 Electrochemical stability

Understanding the electrochemical stability of cathode structures in an aqueous environment during charge and discharge operation is critical to designing new electrode materials with extended operational lifetimes. The equilibrium electrochemical stability of a metal–H₂O system can be inferred from Pourbaix diagrams. For mildly acidic zinc-sulphate electrolyte, the region of interest is pH 3–5⁹⁸ and potential $E_{\pm} \approx E \pm 0.5$ V, where E is the average charge potential given by Eq. (3). The aqueous concentration of TM species of 0.1 M is assumed based on typical concentrations of MnSO₄ used in experimental Zn/MnO₂ battery research.^{8,98,99} Construction of fully *ab initio* Pourbaix diagrams is still out of reach due to difficulties with correlation effects on TM and finite-temperature thermodynamic properties.^{33,100–102} Therefore, we will rely on our analysis of experimental Pourbaix diagrams.

The electrochemical stability of MnO₂ in the context of RAZIBs was recently analysed¹³ and the charge/discharge cycle was mapped on the Mn–H₂O Pourbaix diagram.⁹⁸ MnO₂ is stable at charging potentials, but enters the corrosion region during discharge (Fig. 8a) which limits its stability within the relevant pH/ E_{\pm} window. It is even claimed that some of Zn/MnO₂ capacity can originate from a reversible dissolution of the cathode material.^{11,13,59,60}

α -V₂O₅ stability exists within a narrow range of both pH and potentials (Fig. 8b). Its stability boundaries are extremely sensitive to the concentration of aqueous V species. At

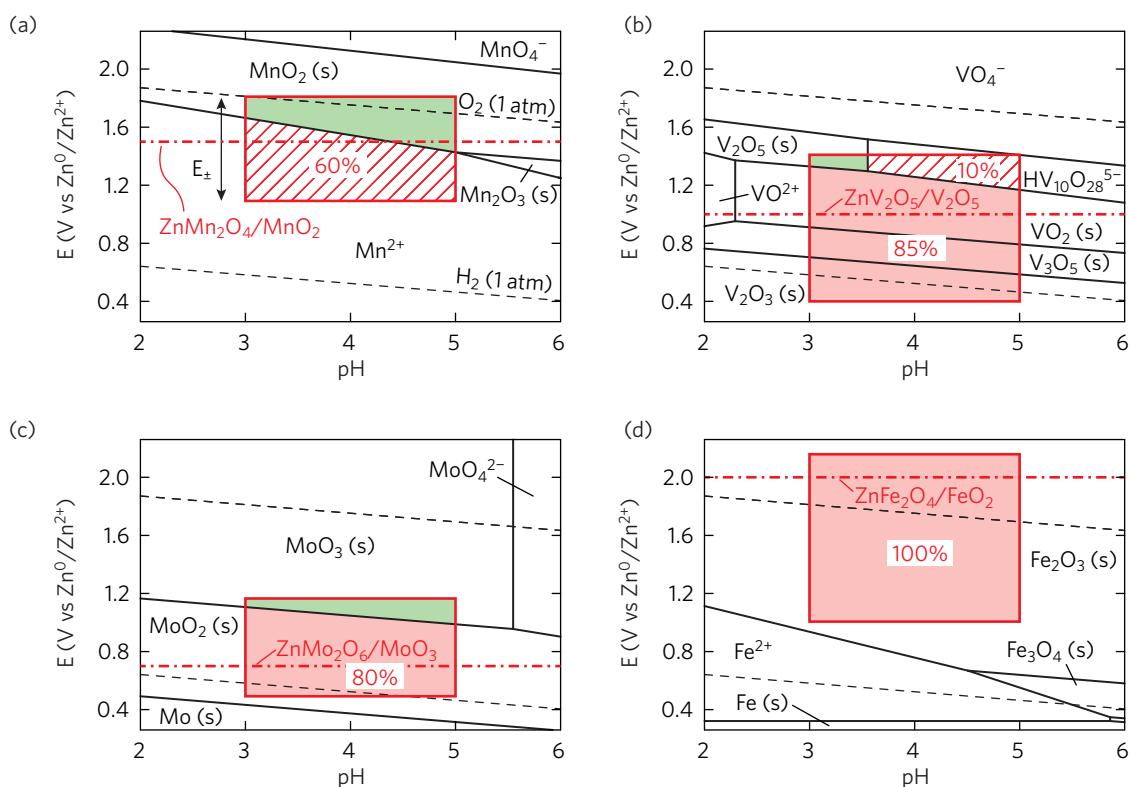


Figure 8: Pourbaix diagrams of (a) Mn–H₂O, (b) V–H₂O, (c) Mo–H₂O, and (d) Fe–H₂O from FactSage thermochemical software.¹⁰³ Concentration of aqueous species is 0.1 M. The red square shows the range of pH and potential during an operating charge/discharge cycle. Within this range the green colour shows boundaries of stability of the pristine (Zn free) cathode material. The pink and hatched areas highlight problematic regions of corrosion and areas where another solid phase (different from the cathode material) is predominant. The percent values indicate a relative share of each area. The red dash-dotted line shows the Zn²⁺ deintercalation potential from Table 5.

the concentration of V aqueous species of 0.1 M, α -V₂O₅ is unstable above pH 3–4 and is prone to corrosion. α -V₂O₅ also becomes unstable at lower potentials $E < 1.2$ – 1.3 V vs Zn⁰/Zn²⁺ in favour of VO₂ (Fig. 8b). The predominance of another solid phase can make the process of dissolution and subsequent re-deposition of the cathode material not fully reversible thereby contributing to capacity fade. Although, Zn/V₂O₅ rechargeable aqueous batteries have a good capacity retention at high current (5 A g⁻¹),¹⁰⁴ the capacity degrades very fast at lower currents (0.1–0.2 A g⁻¹)⁴⁷ due to the cathode dissolution as one of the main factors. Claims of experimental gravimetric energy density (ca. 400 mA h g⁻¹)¹⁰⁴ in the excess of the theoretical limit (300 mA h g⁻¹, Table 5) are not uncommon for Zn/V₂O₅ suggesting a possible contribution of a reversible cathode dissolution to the capacity similar to MnO₂.^{13,59,60}

MoO₃ is stable against corrosion up to pH 5.5 (Fig. 8c). However, MoO₂ takes over the MoO₃ phase at potentials below 0.9–1.0 V vs Zn⁰/Zn²⁺. The predicted charge potential for Zn/MoO₃ is 0.7 V vs Zn⁰/Zn²⁺. Thus, MoO₃ is not stable within the full relevant range of parameters. Experimentally a rapid degradation of Zn/MoO₃ deliverable capacity was observed after the first 1–2 cycles.⁸²

FeO₂ is not present on the Pourbaix diagram (Fig. 8d), which is expected since FeO₂ is unstable. Fe₂O₃ is the only stable solid phase present within the battery operating window, with the discharge potential staying above the corrosion region.

Another important consideration for deployment as cathodes in aqueous zinc ion batteries is the electrochemical stability of aqueous electrolyte against decomposition. It should be noted that the discharge potential for Zn/V₂O₅ and Zn/MoO₃ is bound by the hydrogen evolution line (Fig. 8b,c). The charge potential for Zn/MnO₂ is at the oxygen evolution line, while it dangerously exceeds the oxygen evolution line for Zn/FeO₂ (Fig. 8a,d).

Furthermore, the region of electrochemical stability for α -V₂O₅, MoO₃ and FeO₂ solids does not overlap with the calculated charge potentials (see Fig. 8, dash-dotted lines). Therefore, it is possible to infer that Zn intercalation into the charged cathode will not be a direct

and unopposed reaction as it is desired for battery application. Instead, other solid or aqueous phases will compete for occurring within the operating range of potentials/pH. This shortcoming can lead to a low cycling capability and/or capacity fade due to irreversible cathode decomposition.

Thus, none of the materials analysed fully meet expectations on their electrochemical stability (Table 5), indicating the present challenges in the discovery of suitable host materials. It also highlights the necessity of combining theoretical and experimental efforts for exploring broader material classes in the search for novel RAZIB cathodes.

4 Conclusion

We proposed, verified, and applied a comprehensive set of indicators to screen candidate cathode materials for Zn-ion aqueous rechargeable batteries. The indicators capture feasibility of Zn^{2+} intercalation and transport within the material, the thermodynamic stability of charged and discharged material, electrochemical stability of the cathode material and electrolyte, volume change, and energy storage capacity. Most characteristics can be computed from first principles with the exception of Pourbaix diagrams for the electrochemical stability that currently require experimental inputs. The approach was verified using $\alpha\text{-MnO}_2$ and $\alpha\text{-V}_2\text{O}_5$ as benchmark, the two well studied cathode materials. The screening protocol was applied to MoS_2 , ZrP_2O_7 , MoO_3 , FeO_2 that covered layered, tunnel, and hollow structures to identify alternative cathode materials for Zn-ion aqueous rechargeable batteries. Neither MoS_2 nor ZrP_2O_7 were able to host Zn (had a positive Zn intercalation energy). Other materials (MoO_3 and FeO_2) were able to host Zn, but had other shortcomings (thermodynamic instabilities, charge overpotential leading to electrolyte instabilities, electrochemical instabilities). Electrochemical stability was the most stringent criterion that none of the explored materials were able to meet fully. The second and third most demanding requirements were (i) less than 8% volume change upon Zn intercalation and (ii) thermodynamic stability of the

Zn intercalated structure (not more than 0.16 eV/atom above the energy convex hull). The calculated energy barriers for Zn^{2+} diffusion in $\alpha\text{-V}_2\text{O}_5$ and $\alpha\text{-MnO}_2$ show a large disparity despite both materials demonstrating similar performance as cathodes in RAZIBs. Thus, we are unable to endorse the barrier height as a useful design metric, which is possibly related to competing electrochemical energy storage mechanisms not sensitive to Zn diffusion (e.g., dissolution and subsequent re-deposition of the cathode material in the aqueous electrolyte). While the materials explored in this work did not emerge as promising for application in RAZIBs from a materials property standpoint, the tools and techniques developed in this work can be applied more broadly to screen a wider array of potential material compositions and structures, with the goal of identifying next generation RAZIB cathode materials that can overcome performance and stability shortcoming plaguing this technology for grid scale energy storage applications.

Acknowledgement

O.R. would like to thank Dmitri V. Malakhov (McMaster University) for stimulating discussions regarding electrochemical stability of materials. This work was supported by the Salient Energy, the NSERC Alliance program, and the Mitacs Globalink program. Calculations were performed using the Compute Canada infrastructure supported by the Canada Foundation for Innovation under John R. Evans Leaders Fund.

Supporting Information Available

The raw data (VASP input and structure files) required to reproduce these findings are available in the form Zenodo file repository.¹⁰⁵

References

- (1) Cabana, J.; Monconduit, L.; Larcher, D.; Palacín, M. R. Beyond intercalation-based Li-ion batteries: The state of the art and challenges of electrode materials reacting through conversion reactions. *Adv. Mater.* **2010**, *22*, E170–E192.
- (2) Blanc, L. E.; Kundu, D.; Nazar, L. F. Scientific challenges for the implementation of Zn-ion batteries. *Joule* **2020**, *4*, 771–799.
- (3) Fan, L.; Ma, R.; Wang, J.; Yang, H.; Lu, B. An ultrafast and highly stable potassium-organic battery. *Adv. Mater.* **2018**, *30*, 1805486.
- (4) Pan, Z.; Liu, X.; Yang, J.; Li, X.; Liu, Z.; Loh, X. J.; Wang, J. Aqueous rechargeable multivalent metal-ion batteries: advances and challenges. *Adv. Energy Mater.* **2021**, *11*, 2100608.
- (5) Zhang, N.; Chen, X.; Yu, M.; Niu, Z.; Cheng, F.; Chen, J. Materials chemistry for rechargeable zinc-ion batteries. *Chem. Soc. Rev.* **2020**, *49*, 4203–4219.
- (6) Selvakumaran, D.; Pan, A.; Liang, S.; Cao, G. A review on recent developments and challenges of cathode materials for rechargeable aqueous Zn-ion batteries. *J. Mater. Chem. A* **2019**, *7*, 18209–18236.
- (7) Zhao, Y.; Zhu, Y.; Zhang, X. Challenges and perspectives for manganese-based oxides for advanced aqueous zinc-ion batteries. *InfoMat* **2019**, *2*, 237–260.
- (8) Pan, H.; Shao, Y.; Yan, P.; Cheng, Y.; Han, K. S.; Nie, Z.; Wang, C.; Yang, J.; Li, X.; Bhattacharya, P.; Mueller, K. T.; Liu, J. Reversible aqueous zinc/manganese oxide energy storage from conversion reactions. *Nat. Energy* **2016**, *1*, 16039.
- (9) Chen, L.; An, Q.; Mai, L. Recent advances and prospects of cathode materials for rechargeable aqueous zinc-ion batteries. *Adv. Mater. Interfaces* **2019**, *6*, 1900387.

- (10) Jiang, B.; Xu, C.; Wu, C.; Dong, L.; Li, J.; Kang, F. Manganese sesquioxide as cathode material for multivalent zinc ion battery with high capacity and long cycle life. *Electrochim. Acta* **2017**, *229*, 422–428.
- (11) Wu, D.; Housel, L. M.; Kim, S. J.; Sadique, N.; Quilty, C. D.; Wu, L.; Tappero, R.; Nicholas, S. L.; Ehrlich, S.; Zhu, Y.; Marschilok, A. C.; Takeuchi, E. S.; Bock, D. C.; Takeuchi, K. J. Quantitative temporally and spatially resolved X-ray fluorescence microprobe characterization of the manganese dissolution-deposition mechanism in aqueous Zn/ α -MnO₂ batteries. *Energ. Environ. Sci.* **2020**, *13*, 4322–4333.
- (12) Tran, T. N. T.; Jin, S.; Cuisinier, M.; Adams, B. D.; Ivey, D. G. Reaction mechanisms for electrolytic manganese dioxide in rechargeable aqueous zinc-ion batteries. *Sci. Rep.* **2021**, *11*, 20777.
- (13) Rubel, O.; Tran, T. N. T.; Gourley, S.; Anand, S.; Bommel, A. V.; Adams, B. D.; Ivey, D. G.; Higgins, D. Electrochemical stability of ZnMn₂O₄: Understanding Zn-ion rechargeable battery capacity and degradation. *J. Phys. Chem. C* **2022**, *126*, 10957–10967.
- (14) Chevrier, V. L.; Ong, S. P.; Armiento, R.; Chan, M. K. Y.; Ceder, G. Hybrid density functional calculations of redox potentials and formation energies of transition metal compounds. *Phys. Rev. B* **2010**, *82*, 075122.
- (15) Aydinol, M. K.; Kohan, A. F.; Ceder, G.; Cho, K.; Joannopoulos, J. Ab initio study of lithium intercalation in metal oxides and metal dichalcogenides. *Phys. Rev. B* **1997**, *56*, 1354–1365.
- (16) Zhang, Z.; Zhang, X.; Zhao, X.; Yao, S.; Chen, A.; Zhou, Z. Computational Screening of Layered Materials for Multivalent Ion Batteries. *ACS Omega* **2019**, *4*, 7822–7828.
- (17) Hohenberg, P.; Kohn, W. Inhomogeneous electron gas. *Phys. Rev.* **1964**, *136*, B864–B871.

- (18) Kohn, W.; Sham, L. J. Self-consistent equations including exchange and correlation effects. *Phys. Rev.* **1965**, *140*, A1133–A1138.
- (19) Jain, A.; Ong, S. P.; Hautier, G.; Chen, W.; Richards, W. D.; Dacek, S.; Cholia, S.; Gunter, D.; Skinner, D.; Ceder, G.; Persson, K. A. Commentary: The Materials Project: A materials genome approach to accelerating materials innovation. *APL Mater.* **2013**, *1*, 011002.
- (20) Ong, S. P.; Chevrier, V. L.; Hautier, G.; Jain, A.; Moore, C.; Kim, S.; Ma, X.; Ceder, G. Voltage, stability and diffusion barrier differences between sodium-ion and lithium-ion intercalation materials. *Energ. Environ. Sci.* **2011**, *4*, 3680.
- (21) Le, T.; Sadique, N.; Housel, L. M.; Poyraz, A. S.; Takeuchi, E. S.; Takeuchi, K. J.; Marschilok, A. C.; Liu, P. Discharging behavior of hollandite α -MnO₂ in a hydrated zinc-ion battery. *ACS Appl. Mater. Interfaces* **2021**, *13*, 59937–59949.
- (22) Perdew, J. P.; Burke, K.; Ernzerhof, M. Generalized gradient approximation made simple. *Phys. Rev. Lett.* **1996**, *77*, 3865–3868.
- (23) Luo, H.; Deng, J.; Gou, Q.; Odunmbaku, O.; Sun, K.; Xiao, J.; Li, M.; Zheng, Y. Accelerated discovery of novel high-performance zinc-ion battery cathode materials by combining high-throughput screening and experiments. *Chin. Chem. Lett.* **2022**, 107885.
- (24) Kresse, G.; Hafner, J. Ab initio molecular dynamics for liquid metals. *Phys. Rev. B* **1993**, *47*, 558.
- (25) Kresse, G.; Furthmüller, J. Efficiency of ab-initio total energy calculations for metals and semiconductors using a plane-wave basis set. *Comp. Mater. Sci.* **1996**, *6*, 15–50.
- (26) Kresse, G.; Furthmüller, J. Efficient iterative schemes for ab initio total-energy calculations using a plane-wave basis set. *Phys. Rev. B* **1996**, *54*, 11169–11186.

- (27) Grimme, S.; Antony, J.; Ehrlich, S.; Krieg, H. A consistent and accurate ab initio parametrization of density functional dispersion correction (DFT-D) for the 94 elements H-Pu. *J. Chem. Phys.* **2010**, *132*, 154104.
- (28) Grimme, S.; Ehrlich, S.; Goerigk, L. Effect of the damping function in dispersion corrected density functional theory. *J. Comput. Chem.* **2011**, *32*, 1456–1465.
- (29) Kresse, G.; Joubert, D. From ultrasoft pseudopotentials to the projector augmented-wave method. *Phys. Rev. B* **1999**, *59*, 1758–1775.
- (30) Monkhorst, H. J.; Pack, J. D. Special points for Brillouin-zone integrations. *Phys. Rev. B* **1976**, *13*, 5188–5192.
- (31) Dudarev, S. L.; Botton, G. A.; Savrasov, S. Y.; Humphreys, C. J.; Sutton, A. P. Electron-energy-loss spectra and the structural stability of nickel oxide: An LSDA+U study. *Phys. Rev. B* **1998**, *57*, 1505–1509.
- (32) Capdevila-Cortada, M.; Łodziana, Z.; López, N. Performance of DFT+U Approaches in the Study of Catalytic Materials. *ACS Catal.* **2016**, *6*, 8370–8379.
- (33) Jain, A.; Hautier, G.; Ong, S. P.; Moore, C. J.; Fischer, C. C.; Persson, K. A.; Ceder, G. Formation enthalpies by mixing GGA and GGA+U calculations. *Phys. Rev. B* **2011**, *84*, 045115.
- (34) Jónsson, H.; Mills, G.; Jacobsen, K. W. *Classical and quantum dynamics in condensed phase simulations*; World Scientific, 1998; pp 385–404.
- (35) Mills, G.; Jónsson, H.; Schenter, G. K. Reversible work transition state theory: application to dissociative adsorption of hydrogen. *Surf. Sci.* **1995**, *324*, 305–337.
- (36) Thermodynamic Properties of Compounds, LiO to MnS₂: Datasheet from Landolt-Börnstein - Group IV Physical Chemistry - Volume 19A4: “Pure Substances. Part 4 - Compounds from HgH.g to ZnTe.g” in SpringerMaterials

(https://doi.org/10.1007/10688868_10). 2001; https://materials.springer.com/lb/docs/sm_lbs_978-3-540-45274-4_10.

- (37) Franchini, C.; Podloucky, R.; Paier, J.; Marsman, M.; Kresse, G. Ground-state properties of multivalent manganese oxides: Density functional and hybrid density functional calculations. *Phys. Rev. B* **2007**, *75*, 195128.
- (38) Eckhoff, M.; Blöchl, P. E.; Behler, J. Hybrid density functional theory benchmark study on lithium manganese oxides. *Phys. Rev. B* **2020**, *101*, 205113.
- (39) Chase, M. W. NIST-JANAF Thermochemical Tables, 4th Edition. *J. Phys. Chem. Ref. Data* **1998**, *Monograph 9*, 1–1951.
- (40) Das, T.; Tosoni, S.; Pacchioni, G. Structural and electronic properties of bulk and ultrathin layers of V_2O_5 and MoO_3 . *Comp. Mater. Sci.* **2019**, *163*, 230–240.
- (41) Brown, P. L.; Curti, E.; Grambow, B.; Ekberg, C. *Chemical thermodynamics of zirconium*; Elsevier Amsterdam, 2005; Vol. 8.
- (42) Wu, X.; Kang, F.; Duan, W.; Li, J. Density functional theory calculations: A powerful tool to simulate and design high-performance energy storage and conversion materials. *Prog. Nat. Sci. Mater. Int.* **2019**, *29*, 247–255.
- (43) Xu, C.; Li, B.; Du, H.; Kang, F. Energetic zinc ion chemistry: The rechargeable zinc ion battery. *Angew. Chem. Int. Ed.* **2011**, *51*, 933–935.
- (44) Alfaruqi, M. H.; Mathew, V.; Gim, J.; Kim, S.; Song, J.; Baboo, J. P.; Choi, S. H.; Kim, J. Electrochemically Induced Structural Transformation in a γ - MnO_2 Cathode of a High Capacity Zinc-Ion Battery System. *Chem. Mater.* **2015**, *27*, 3609–3620.
- (45) Kundu, D.; Adams, B. D.; Duffort, V.; Vajargah, S. H.; Nazar, L. F. A high-capacity and long-life aqueous rechargeable zinc battery using a metal oxide intercalation cathode. *Nat. Energy* **2016**, *1*, 4599.

- (46) Song, M.; Tan, H.; Chao, D.; Fan, H. J. Recent Advances in Zn-Ion Batteries. *Adv. Funct. Mater.* **2018**, *28*, 1802564.
- (47) Yang, G.; Li, Q.; Ma, K.; Hong, C.; Wang, C. The degradation mechanism of vanadium oxide-based aqueous zinc-ion batteries. *J. Mater. Chem. A* **2020**, *8*, 8084–8095.
- (48) Byeon, P.; Hong, Y.; Bae, H. B.; Shin, J.; Choi, J. W.; Chung, S.-Y. Atomic-scale unveiling of multiphase evolution during hydrated Zn-ion insertion in vanadium oxide. *Nat. Commun.* **2021**, *12*, 4599.
- (49) Haas, P.; Tran, F.; Blaha, P. Calculation of the lattice constant of solids with semilocal functionals. *Phys. Rev. B* **2009**, *79*, 085104.
- (50) PAULING FILE Multinaries Edition in SpringerMaterials. 2016; <https://materials.springer.com>, Copyright 2016 Springer-Verlag Berlin Heidelberg & Material Phases Data System (MPDS), Switzerland & National Institute for Materials Science (NIMS), Japan.
- (51) Wang, L.; Maxisch, T.; Ceder, G. Oxidation energies of transition metal oxides within the GGA + U framework. *Phys. Rev. B* **2006**, *73*, 195107.
- (52) Urban, A.; Seo, D.-H.; Ceder, G. Computational understanding of Li-ion batteries. *npj Comput. Mater.* **2016**, *2*, 16002.
- (53) Wu, X.; Xiang, Y.; Peng, Q.; Wu, X.; Li, Y.; Tang, F.; Song, R.; Liu, Z.; He, Z.; Wu, X. Green-low-cost rechargeable aqueous zinc-ion batteries using hollow porous spinel ZnMn_2O_4 as the cathode material. *J. Mater. Chem. A* **2017**, *5*, 17990–17997.
- (54) Tang, Z.; Chen, W.; Lyu, Z.; Chen, Q. Size-Dependent Reaction Mechanism of λ - MnO_2 Particles as Cathodes in Aqueous Zinc-Ion Batteries. *Energy Mater. Adv.* **2022**, *2022*, 9765710.

- (55) Alfaruqi, M. H.; Gim, J.; Kim, S.; Song, J.; Jo, J.; Kim, S.; Mathew, V.; Kim, J. Enhanced reversible divalent zinc storage in a structurally stable α -MnO₂ nanorod electrode. *J. Power Sources* **2015**, *288*, 320–327.
- (56) Lee, B.; Lee, H. R.; Kim, H.; Chung, K. Y.; Cho, B. W.; Oh, S. H. Elucidating the intercalation mechanism of zinc ions into α -MnO₂ for rechargeable zinc batteries. *Chem. Commun.* **2015**, *51*, 9265–9268.
- (57) Pang, Q.; He, W.; Yu, X.; Yang, S.; Zhao, H.; Fu, Y.; Xing, M.; Tian, Y.; Luo, X.; Wei, Y. Aluminium pre-intercalated orthorhombic V₂O₅ as high-performance cathode material for aqueous zinc-ion batteries. *Appl. Surf. Sci.* **2021**, *538*, 148043.
- (58) Hu, P.; Yan, M.; Zhu, T.; Wang, X.; Wei, X.; Li, J.; Zhou, L.; Li, Z.; Chen, L.; Mai, L. Zn/V₂O₅ Aqueous Hybrid-Ion Battery with High Voltage Platform and Long Cycle Life. *ACS Appl. Mater. Interfaces* **2017**, *9*, 42717–42722.
- (59) Lee, B.; Yoon, C. S.; Lee, H. R.; Chung, K. Y.; Cho, B. W.; Oh, S. H. Electrochemically-induced reversible transition from the tunneled to layered polymorphs of manganese dioxide. *Sci. Rep.* **2014**, *4*, 6066.
- (60) Moon, H.; Ha, K.-H.; Park, Y.; Lee, J.; Kwon, M.-S.; Lim, J.; Lee, M.-H.; Kim, D.-H.; Choi, J. H.; Choi, J.-H.; Lee, K. T. Direct proof of the reversible dissolution/deposition of Mn²⁺/Mn⁴⁺ for mild-acid Zn-MnO₂ batteries with porous carbon interlayers. *Adv. Sci.* **2021**, *8*, 2003714.
- (61) Chen, H.; Dai, C.; Xiao, F.; Yang, Q.; Cai, S.; Xu, M.; Fan, H. J.; Bao, S.-J. Reunderstanding the reaction mechanism of aqueous Zn-Mn batteries with sulfate electrolytes: Role of the zinc sulfate hydroxide. *Adv. Mater.* **2022**, *34*, 2109092.
- (62) Jiao, Y.; Kang, L.; Berry-Gair, J.; McColl, K.; Li, J.; Dong, H.; Jiang, H.; Wang, R.; Corà, F.; Brett, D. J. L.; He, G.; Parkin, I. P. Enabling stable MnO₂ matrix for aqueous zinc-ion battery cathodes. *J. Mater. Chem. A* **2020**, *8*, 22075–22082.

- (63) Gautam, G. S.; Canepa, P.; Malik, R.; Liu, M.; Persson, K.; Ceder, G. First-principles evaluation of multi-valent cation insertion into orthorhombic V_2O_5 . *Chem. Commun.* **2015**, *51*, 13619–13622.
- (64) Sandagiripathira, K.; Moghaddasi, M. A.; Shepard, R.; Smeu, M. Investigating the role of structural water on the electrochemical properties of α - V_2O_5 through density functional theory. *Phys. Chem. Chem. Phys.* **2022**, *24*, 24271–24280.
- (65) Horrocks, G. A.; Likely, M. F.; Velazquez, J. M.; Banerjee, S. Finite size effects on the structural progression induced by lithiation of V_2O_5 : a combined diffraction and Raman spectroscopy study. *J. Mater. Chem. A* **2013**, *1*, 15265.
- (66) Gautam, G. S.; Canepa, P.; Abdellahi, A.; Urban, A.; Malik, R.; Ceder, G. The intercalation phase diagram of Mg in V_2O_5 from first-principles. *Chem. Mater.* **2015**, *27*, 3733–3742.
- (67) Putro, D. Y.; Alfaruqi, M. H.; Islam, S.; Kim, S.; Park, S.; Lee, S.; Hwang, J.-Y.; Sun, Y.-K.; Kim, J. Quasi-solid-state zinc-ion battery based on α - MnO_2 cathode with husk-like morphology. *Electrochim. Acta* **2020**, *345*, 136189.
- (68) Rong, Z.; Malik, R.; Canepa, P.; Sai Gautam, G.; Liu, M.; Jain, A.; Persson, K.; Ceder, G. Materials design rules for multivalent ion mobility in intercalation structures. *Chem. Mater.* **2015**, *27*, 6016–6021.
- (69) Yi, T.-F.; Qiu, L.; Qu, J.-P.; Liu, H.; Zhang, J.-H.; Zhu, Y.-R. Towards high-performance cathodes: Design and energy storage mechanism of vanadium oxides-based materials for aqueous Zn-ion batteries. *Coord. Chem. Rev.* **2021**, *446*, 214124.
- (70) Slater, J. C. Atomic Radii in Crystals. *J. Chem. Phys.* **1964**, *41*, 3199–3204.
- (71) Downs, R. T.; Hall-Wallace, M. The american mineralogist crystal structure database. *Am. Mineral.* **2003**, *88*, 247–250.

- (72) Gražulis, S.; Chateigner, D.; Downs, R. T.; Yokochi, A. F. T.; Quirós, M.; Lutterotti, L.; Manakova, E.; Butkus, J.; Moeck, P.; Bail, A. L. Crystallography Open Database—an open-access collection of crystal structures. *J. Appl. Crystallogr.* **2009**, *42*, 726–729.
- (73) Gražulis, S.; Daškevič, A.; Merkys, A.; Chateigner, D.; Lutterotti, L.; Quirós, M.; Serebryanaya, N. R.; Moeck, P.; Downs, R. T.; Bail, A. L. Crystallography Open Database (COD): an open-access collection of crystal structures and platform for world-wide collaboration. *Nucleic Acids Res.* **2011**, *40*, D420–D427.
- (74) Shin, J.; Choi, D. S.; Lee, H. J.; Jung, Y.; Choi, J. W. Hydrated Intercalation for High-Performance Aqueous Zinc Ion Batteries. *Adv. Energy Mater.* **2019**, *9*, 1900083.
- (75) Adams, B. D.; Brown, R. D.; Cuisinier, M.; Jin, S. Layered electrode materials and methods for rechargeable zinc batteries. 2020; patent US 2020/0395606 A1.
- (76) Hou, Z.; Tan, H.; Gao, Y.; Li, M.; Lu, Z.; Zhang, B. Tailoring desolvation kinetics enables stable zinc metal anodes. *J. Mater. Chem. A* **2020**, *8*, 19367–19374.
- (77) Cauët, E.; Bogatko, S.; Weare, J. H.; Fulton, J. L.; Schenter, G. K.; Bylaska, E. J. Structure and dynamics of the hydration shells of the Zn^{2+} ion from *ab initio* molecular dynamics and combined *ab initio* and classical molecular dynamics simulations. *J. Chem. Phys.* **2010**, *132*, 194502.
- (78) Brady, A. B.; Tallman, K. R.; Takeuchi, E. S.; Marschilok, A. C.; Takeuchi, K. J.; Liu, P. Transition metal substitution of hollandite $\alpha\text{-MnO}_2$: enhanced potential and structural stability on lithiation from first-principles calculation. *J. Phys. Chem. C* **2019**, *123*, 25042–25051.
- (79) Post, J. E.; Heaney, P. J.; Dreele, R. B. V.; Hanson, J. C. Neutron and temperature-resolved synchrotron X-ray powder diffraction study of akaganéite. *Am. Mineral.* **2003**, *88*, 782–788.

- (80) Fernandez-Martinez, A.; Timon, V.; Roman-Ross, G.; Cuello, G. J.; Daniels, J. E.; Ayora, C. The structure of schwertmannite, a nanocrystalline iron oxyhydroxysulfate. *Am. Mineral.* **2010**, *95*, 1312–1322.
- (81) Zhang, Y.; Pelliccione, C. J.; Brady, A. B.; Guo, H.; Smith, P. F.; Liu, P.; Marschilok, A. C.; Takeuchi, K. J.; Takeuchi, E. S. Probing the Li insertion mechanism of ZnFe_2O_4 in Li-ion batteries: a combined x-ray diffraction, extended x-ray absorption fine structure, and density functional theory study. *Chem. Mater.* **2017**, *29*, 4282–4292.
- (82) Liu, W.; Hao, J.; Xu, C.; Mou, J.; Dong, L.; Jiang, F.; Kang, Z.; Wu, J.; Jiang, B.; Kang, F. Investigation of zinc ion storage of transition metal oxides, sulfides, and borides in zinc ion battery systems. *Chem. Commun.* **2017**, *53*, 6872–6874.
- (83) Lee, W. S. V.; Xiong, T.; Wang, X.; Xue, J. Unraveling MoS_2 and transition metal dichalcogenides as functional zinc-ion battery cathode: a perspective. *Small Methods* **2020**, *5*, 2000815.
- (84) Li, Y.; Zhang, R.; Zhou, W.; Wu, X.; Zhang, H.; Zhang, J. Hierarchical MoS_2 hollow architectures with abundant Mo vacancies for efficient sodium storage. *ACS Nano* **2019**, *13*, 5533–5540.
- (85) Liu, L.; Yang, W.; Chen, H.; Chen, X.; Zhang, K.; Zeng, Q.; Lei, S.; Huang, J.; Li, S.; Peng, S. High zinc-ion intercalation reaction activity of MoS_2 cathode based on regulation of thermodynamic metastability and interlayer water. *Electrochim. Acta* **2022**, *410*, 140016.
- (86) Liu, X. H.; Zhong, L.; Huang, S.; Mao, S. X.; Zhu, T.; Huang, J. Y. Size-dependent fracture of silicon nanoparticles during lithiation. *ACS Nano* **2012**, *6*, 1522–1531.
- (87) de Biasi, L.; Lieser, G.; Dräger, C.; Indris, S.; Rana, J.; Schumacher, G.; Mönig, R.;

- Ehrenberg, H.; Binder, J. R.; Geßwein, H. LiCaFeF₆: A zero-strain cathode material for use in Li-ion batteries. *J. Power Sources* **2017**, *362*, 192–201.
- (88) Moorhead-Rosenberg, Z.; Harrison, K. L.; Turner, T.; Manthiram, A. A rapid microwave-assisted solvothermal approach to lower-valent transition metal oxides. *Inorg. Chem.* **2013**, *52*, 13087–13093.
- (89) Wu, T.; Zhu, K.; Qin, C.; Huang, K. Unraveling the role of structural water in bilayer V₂O₅ during Zn²⁺-intercalation: insights from DFT calculations. *J. Mater. Chem. A* **2019**, *7*, 5612–5620.
- (90) Ong, S. P.; Wang, L.; Kang, B.; Ceder, G. Li-Fe-P-O₂ phase diagram from first principles calculations. *Chem. Mater.* **2008**, *20*, 1798–1807.
- (91) Predel, B. Mo-O (Molybdenum-Oxygen): Datasheet from Landolt-Börnstein - Group IV Physical Chemistry - Volume 5H: “Li-Mg – Nd-Zr” in SpringerMaterials (https://doi.org/10.1007/10522884_2076). 1997; https://materials.springer.com/lb/docs/sm_lbs_978-3-540-68538-8_2076, Copyright 1997 Springer-Verlag Berlin Heidelberg.
- (92) Reichelt, W.; Weber, T.; Söhnel, T.; Däbritz, S. Mischkristallbildung im System CuMoO₄/ZnMoO₄. *Z. Anorg. Allg. Chem.* **2000**, *626*, 2020–2027.
- (93) Söhnel, T.; Reichelt, W.; Oppermann, H. Zum System Zn/Mo/O. II. Chemischer Transport ternärer Zinkmolybdate. *Z. Anorg. Allg. Chem.* **1997**, *623*, 1190–1200.
- (94) Kubaschewski, O.; Schmid-Fetzer, R. Temperature - composition phase diagram of the Fe-O system: Datasheet from MSI Eureka in SpringerMaterials (https://materials.springer.com/msi/phase-diagram/docs/sm_msi_r_10_011481_02_full_LnkDia2). 2007; https://materials.springer.com/msi/phase-diagram/docs/sm_msi_r_10_011481_02_full_LnkDia2, Copyright 2007 MSI, Materials Science International Services GmbH, Stuttgart.

- (95) Hu, Q.; Kim, D. Y.; Yang, W.; Yang, L.; Meng, Y.; Zhang, L.; Mao, H.-K. FeO₂ and FeOOH under deep lower-mantle conditions and Earth's oxygen-hydrogen cycles. *Nature* **2016**, *534*, 241–244.
- (96) Watson, A.; Chang, K.; Dang, S.; Gotcu-Freis, P.; Khvan, A.; Markus, T.; Schuster, E.; Strafela, M. Co-Li-O ternary phase diagram evaluation: Datasheet from MSI Eureka in SpringerMaterials (dataset ID: sm_msi_r_10_029498_01). 2016; https://materials.springer.com/msi/docs/sm_msi_r_10_029498_01.
- (97) Chang, K. Phase equilibria, thermodynamic and electrochemical properties of cathodes in lithium ion batteries based on the Li-(Co, Ni)-O system. Ph.D. thesis, Rheinisch-Westfälischen Technischen Hochschule Aachen, 2013.
- (98) Bischoff, C. F.; Fitz, O. S.; Burns, J.; Bauer, M.; Gentischer, H.; Birke, K. P.; Henning, H.-M.; Biro, D. Revealing the local pH value changes of acidic aqueous zinc ion batteries with a manganese dioxide electrode during cycling. *J. Electrochem. Soc.* **2020**, *167*, 020545.
- (99) Chamoun, M.; Brant, W. R.; Tai, C.-W.; Karlsson, G.; Noréus, D. Rechargeability of aqueous sulfate Zn/MnO₂ batteries enhanced by accessible Mn²⁺ ions. *Energy Stor. Mater.* **2018**, *15*, 351–360.
- (100) Persson, K. A.; Waldwick, B.; Lazic, P.; Ceder, G. Prediction of solid-aqueous equilibria: Scheme to combine first-principles calculations of solids with experimental aqueous states. *Phys. Rev. B* **2012**, *85*, 235438.
- (101) Zeng, Z.; Chan, M. K. Y.; Zhao, Z.-J.; Kubal, J.; Fan, D.; Greeley, J. Towards first principles-based prediction of highly accurate electrochemical Pourbaix diagrams. *J. Phys. Chem. C* **2015**, *119*, 18177–18187.
- (102) Wang, Z.; Guo, X.; Montoya, J.; Nørskov, J. K. Predicting aqueous stability of solid

- with computed Pourbaix diagram using SCAN functional. *npj Comput. Mater.* **2020**, *6*, 160.
- (103) Bale, C. W.; B elisle, E.; Chartrand, P.; Deckerov, S. A.; Eriksson, G.; Gheribi, A. E.; Hack, K.; Jung, I.-H.; Kang, Y.-B.; Melan on, J.; Pelton, A. D.; Petersen, S.; Robelin, C.; Sangster, J.; Spencer, P.; Ende, M.-A. V. FactSage thermochemical software and databases, 2010–2016. *Calphad* **2016**, *54*, 35–53.
- (104) Zhang, N.; Dong, Y.; Jia, M.; Bian, X.; Wang, Y.; Qiu, M.; Xu, J.; Liu, Y.; Jiao, L.; Cheng, F. Rechargeable aqueous Zn-V₂O₅ battery with high energy density and long cycle life. *ACS Energy Lett.* **2018**, *3*, 1366–1372.
- (105) Anand, S.; Miliante, C. M.; Storm, G.; Adams, B. D.; Higgins, D.; Rubel, O. Computational screening of cathode materials for Zn-ion rechargeable batteries (supporting files). <https://zenodo.org/record/7796317>, 2023; <https://zenodo.org/record/7796317>, Zenado file repository, doi: 10.5281/zenodo.7796317.

Graphical TOC Entry

